






**Two-gap time reversal symmetry breaking superconductivity in noncentrosymmetric LaNiC<sub>2</sub>**Shyam Sundar <sup>1</sup>, S. R. Dunsiger,<sup>1,2</sup> S. Gheidi,<sup>1</sup> K. S. Akella,<sup>1</sup> A. M. Côté,<sup>1</sup> H. U. Özdemir,<sup>1</sup> N. R. Lee-Hone <sup>1</sup>, D. M. Broun,<sup>1</sup> E. Mun <sup>1</sup>, F. Honda,<sup>3</sup> Y. J. Sato,<sup>3</sup> T. Koizumi,<sup>3</sup> R. Settai,<sup>4</sup> Y. Hirose,<sup>4</sup> I. Bonalde <sup>5</sup> and J. E. Sonier <sup>1</sup><sup>1</sup>*Department of Physics, Simon Fraser University, Burnaby, British Columbia, Canada V5A 1S6*<sup>2</sup>*Centre for Molecular and Materials Science, TRIUMF, Vancouver, British Columbia, Canada V6T 2A3*<sup>3</sup>*Institute for Materials Research, Tohoku University, Oarai, Ibaraki 311-1313, Japan*<sup>4</sup>*Department of Physics, Niigata University, Niigata 950-2181, Japan*<sup>5</sup>*Centro de Física, Instituto Venezolano de Investigaciones Científicas, Apartado 20632, Caracas 1020-A, Venezuela*

(Received 3 June 2020; revised 21 December 2020; accepted 11 January 2021; published 20 January 2021)

We report a  $\mu$ SR investigation of a noncentrosymmetric superconductor (LaNiC<sub>2</sub>) in single-crystal form. Compared to previous  $\mu$ SR studies of noncentrosymmetric superconducting polycrystalline and powder samples, the unambiguous orientation of single crystals enables a simultaneous determination of the absolute value of the magnetic penetration depth and the vortex core size from measurements that probe the magnetic field distribution in the vortex state. The magnetic field dependence of these quantities unambiguously demonstrates the presence of two nodeless superconducting energy gaps. In addition, we detect weak internal magnetic fields in the superconducting phase, confirming earlier  $\mu$ SR evidence for a time-reversal symmetry-breaking superconducting state. Our results suggest that Cooper pairing in LaNiC<sub>2</sub> is characterized by an interorbital equal-spin pairing model introduced to unify the pairing states of LaNiC<sub>2</sub> and the centrosymmetric superconductor LaNiGa<sub>2</sub>.

DOI: [10.1103/PhysRevB.103.014511](https://doi.org/10.1103/PhysRevB.103.014511)**I. INTRODUCTION**

While the formation of Cooper pairs in a superconductor is generally protected by time-reversal and inversion symmetries, superconductivity is also exhibited by certain materials lacking a center of inversion in their crystal structure. These so-called noncentrosymmetric superconductors (NCSCs) have garnered a great deal of attention in the past decade. The lack of inversion symmetry enables an anti-symmetric spin-orbit coupling (ASOC) of the single electron states, which facilitates mixing of spin-singlet and spin-triplet configurations in the superconducting (SC) pair wave function [1,2]. The degree of mixing is in part dependent on the strength of the ASOC.

There is evidence from zero-field (ZF)  $\mu$ SR measurements that the SC states of some NCSCs break time-reversal symmetry (TRS) [3–12]. Such appears to be the case for the noncentrosymmetric ternary carbide compound LaNiC<sub>2</sub>, where measurements on a polycrystalline sample show a weak increase in the ZF- $\mu$ SR relaxation rate at the SC transition temperature ( $T_c$ ) indicative of the formation of spontaneous magnetic fields [3]. The only TRS breaking states permitted by the low point-group symmetry ( $C_{2v}$ ) of the orthorhombic crystal structure of LaNiC<sub>2</sub> are those with nonunitary spin-triplet pairing [13,14]. These allowed pairing states are incompatible with strong ASOC and appreciable singlet-triplet mixing, and have nodes in the associated SC energy-gap function [13,14]. However, different experiments have reached very different conclusions regarding the energy-gap structure in LaNiC<sub>2</sub>. While initial specific-heat measurements suggested an unconventional SC gap with

point nodes [15], a conventional isotropic BCS  $s$ -wave gap is supported by subsequent specific-heat [16] and nuclear quadrupole resonance [17] studies, as well as a strong suppression of  $T_c$  by Ce substitution for La [18]. There is also evidence for the existence of two nodeless SC gaps in LaNiC<sub>2</sub> from specific-heat measurements and changes in the magnetic penetration depth with temperature,  $\Delta\lambda(T)$ , measured in the Meissner state via a tunnel diode oscillator technique [19]. Still other measurements of  $\Delta\lambda(T)$  by the same method support the earlier claim of point nodes in the SC energy gap [20,21].

To explain experiments on LaNiC<sub>2</sub> and the centrosymmetric superconductor LaNiGa<sub>2</sub> that indicate TRS breaking and fully gapped behavior, a nonunitary triplet SC pairing state has been proposed in which pairing occurs between electrons of the same spin, but on two different orbitals [22,23]. Depending on the character of the two orbitals involved in this interorbital equal-spin pairing (ESP) state, two nodeless SC energy gaps associated with the two different values of the Cooper pair spin ( $S_z = +1$  and  $-1$ ) may exist. If the ESP occurs between electrons on different orbitals of the Ni atom, a gap with line nodes or a single anisotropic SC energy gap may occur [24]. Only the latter requires the noncentrosymmetric crystal structure of LaNiC<sub>2</sub>.

In this paper, we resolve the question of the SC gap structure in LaNiC<sub>2</sub> via  $\mu$ SR measurements of single crystals in the vortex state. Two-gap superconductivity is unambiguously identified in the magnetic field dependence of the fitted values of the absolute value of the magnetic penetration depth ( $\lambda$ ) and the vortex core size. To date all evidence of TRS breaking in NCSCs by ZF- $\mu$ SR has come from experiments

on powder or polycrystalline samples via the observation of an increase in the relaxation rate at  $T_c$ , which is rather small compared to that detected in single crystals of TRS breaking centrosymmetric superconductors  $\text{UPt}_3$  [25],  $\text{Sr}_2\text{RuO}_4$  [26], and  $\text{PrOs}_4\text{Sb}_{12}$  [27]. Here we also report evidence for TRS breaking in  $\text{LaNiC}_2$  single crystals by the detection of weak internal magnetic fields below  $T_c$ .

## II. EXPERIMENTAL DETAILS

Single crystals of  $\text{LaNiC}_2$  were grown by the Czochralski method, as described in Ref. [28]. Heat-capacity and magnetization measurements indicate that bulk superconductivity occurs with a ZF value  $T_c \sim 2.7$  K and an upper critical magnetic field  $H_{c2}^{\parallel a} \sim 1.53$  kOe (see Appendix C). A secondary phase of  $\text{La}_2\text{Ni}_5\text{C}_3$  identified by x-ray diffraction (see Appendix A) is present in  $\approx 5\%$  of the sample volume, but is nonsuperconducting down to at least 0.11 K (see Fig. 8, Appendix B).

The  $\mu\text{SR}$  experiments were performed on the M15 surface muon beamline at TRIUMF using a top loading dilution refrigerator. A mosaic of seven  $a$ -axis aligned  $\text{LaNiC}_2$  single crystals, each  $\approx 0.5$  mm thick and six having a mass of  $\approx 70$  mg each, were mounted on a  $12.5 \times 22 \times 0.25$  mm pure Ag plate and attached to an Ag sample holder. Together, the  $\text{LaNiC}_2$  single crystals covered  $\approx 70\%$  of the Ag plate [see Fig. 1(b) inset]. Measurements in the vortex state were performed in a transverse-field (TF) geometry [29], with the magnetic field applied parallel to the  $a$  axis of the  $\text{LaNiC}_2$  single crystals and transverse to the initial muon-spin polarization  $\mathbf{P}(t=0)$ . The field was first applied above  $T_c$  before cooling into the vortex state. To reduce the contribution to the TF- $\mu\text{SR}$  signal from muons stopping in the Ag backing plate, three thin wafers of intrinsic GaAs were used to cover the exposed area around the  $\text{LaNiC}_2$  sample—GaAs produces no detectable muon precession signal for the field range considered in our paper. No GaAs was used for the ZF measurements, as this would give rise to a relaxing signal associated with muonium ( $\text{Mu} \equiv \mu^+e^-$ ) formation. Conversely, the very small Ag nuclear moments produce no appreciable relaxation of the ZF- $\mu\text{SR}$  signal. For the ZF- $\mu\text{SR}$  experiments,  $\mathbf{P}(t=0)$  was parallel to the  $a$  axis and stray external magnetic fields at the sample position were reduced to  $\lesssim 35$  mG using field compensation coils and the precession signal of Mu in intrinsic Si as a sensitive magnetometer [30].

## III. RESULTS AND DISCUSSION

Figure 1(a) shows representative TF- $\mu\text{SR}$  asymmetry spectra  $A(t)$  displayed in a rotating reference frame. The significant damping of the signal below  $T_c$  is due to muons randomly sampling the spatial distribution of magnetic field associated with a vortex lattice (VL). Gaussian apodized Fourier transforms (FTs) of the TF- $\mu\text{SR}$  signals are shown in Fig. 1(b) and Appendix E (Figs. 12 and 13). The FT is representative of the magnetic field distribution  $n(B)$  sensed by muons stopping inside and outside the sample, but is broadened by the apodization used to smooth out the ringing and noise artifacts caused by the finite time range and the reduced number of muon decay events at long times [29]. The FT

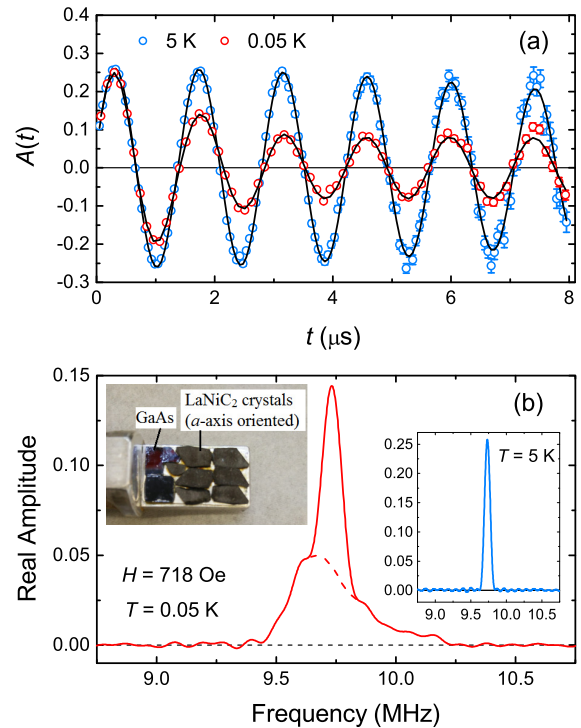


FIG. 1. (a) TF- $\mu\text{SR}$  asymmetry spectra recorded above and below  $T_c$  for a magnetic field of  $H = 718$  Oe displayed in a 9.03-MHz rotating reference frame. Note, the precession frequency is related to the local field by  $\nu = (\gamma_\mu/2\pi)B$ , where  $\gamma_\mu/2\pi = 13.5539$  MHz/kG is the muon gyromagnetic ratio. Also shown are fits that use Eq. (1) below  $T_c$  (see Appendix D). (b) Fourier transform of the TF- $\mu\text{SR}$  signal for  $T = 0.05$  K. The large peak at 9.73 MHz is due to muons stopping outside the sample. Left inset: Photograph of the  $\text{LaNiC}_2$  single crystals and GaAs wafers attached to an Ag backing plate on an Ag sample holder. Right inset: Fourier transform of TF- $\mu\text{SR}$  signal for  $T = 5$  K.

below  $T_c$  shows a large peak due to muons stopping in the Ag backing plate or sample holder, superimposed on an asymmetric line shape generated by muons sensing the nuclear moments and VL in the  $\text{LaNiC}_2$  single crystals. Below  $T_c$ , the VL contribution to  $A(t)$  (see Appendix D) is well described by the following analytical Ginzburg-Landau (GL) model for the spatial variation of field generated by a hexagonal VL [31]:

$$B(\mathbf{r}) = B_0(1 - b^4) \sum_{\mathbf{G}} \frac{e^{-i\mathbf{G}\cdot\mathbf{r}} u K_1(u)}{\lambda_{bc}^2 G^2}, \quad (1)$$

where  $b = B/B_{c2}$  is the ratio of the local and upper critical magnetic fields,  $B_0$  is the average internal magnetic field,  $\mathbf{G}$  are the VL reciprocal-lattice vectors,  $K_1(u)$  is a modified Bessel function,  $u^2 = 2\xi_{bc}^2 G^2(1 + b^4)[1 - 2b(1 - b^2)]$ , and  $\xi_{bc}$  and  $\lambda_{bc}$  are the coherence length and magnetic penetration depth associated with supercurrents flowing in the  $bc$  plane. The suitability of Eq. (1) has been widely demonstrated in previous  $\mu\text{SR}$  investigations of type-II superconductors, where the vortex core size ( $r_0$ ) is defined as the radial distance from the vortex center to the maximum in the absolute value of the supercurrent density  $j(r) = |\nabla \times \mathbf{B}(r)|$  [32,33]. Since changes in the slope of the pair potential  $\Delta(r)$  in the vortex core region modify the cutoff factor  $uK_1(u)$  in Eq. (1), changes in the

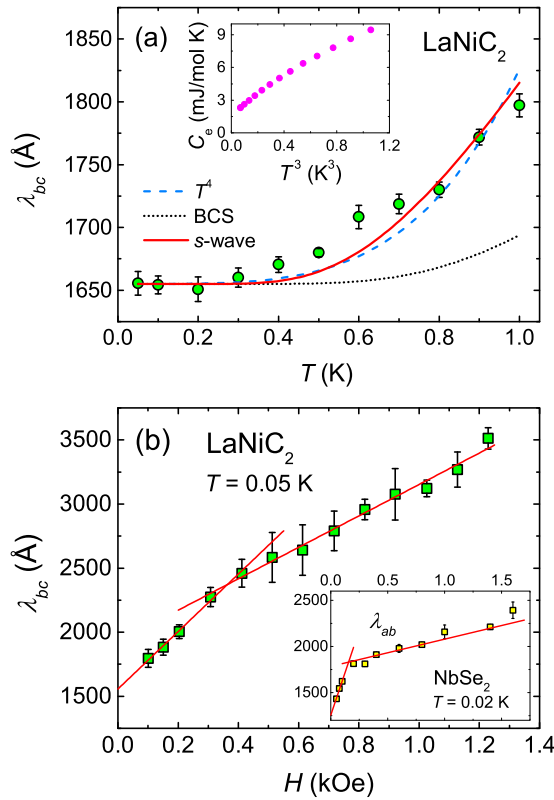


FIG. 2. (a) Temperature dependence of  $\lambda_{bc}$  in  $\text{LaNiC}_2$  below  $T \sim 0.38T_c$  and for  $H = 150$  Oe. The dashed curve is a fit of the form  $\lambda_{bc}(0) + aT^4$  expected for point nodes along the  $a$  axis. The dotted and solid curves are fits to the single-gap  $s$ -wave BCS expression [34] with zero-temperature energy-gap values  $\Delta_{bc}(0) = 1.76k_B T_c$  and  $\Delta_{bc}(0) = 1.16(3)k_B T_c$ , respectively. Inset: Low-temperature ( $0.41 \text{ K} \leq T \leq 1 \text{ K}$ ) electronic contribution to the heat capacity plotted vs  $T^3$ . (b) Magnetic field dependence of  $\lambda_{bc}$  in  $\text{LaNiC}_2$  for  $T = 0.05 \text{ K}$ . The straight lines are linear fits for  $H \leq 0.4 \text{ kOe}$  and  $H \geq 0.5 \text{ kOe}$ . The fit for  $H \leq 0.4 \text{ kOe}$  yields the ZF value  $\lambda_{bc}(0) = 1548 \pm 24 \text{ \AA}$ . Inset: Magnetic field dependence of  $\lambda_{ab}$  in  $\text{NbSe}_2$  for  $T = 0.02 \text{ K}$  [35].

core size modify the fitted value of  $\xi_{bc}$  [33]. Consequently, the “true” GL coherence length is the value of  $\xi_{bc}$  in the  $T \rightarrow 0$  and  $H \rightarrow 0$  limits.

Figure 2(a) shows the temperature dependence of  $\lambda_{bc}$  obtained from fits of TF- $\mu$ SR spectra recorded for  $H = 150$  Oe and  $T \leq 1 \text{ K}$ . The data are poorly described by the form  $\lambda_{bc}(T) - \lambda_{bc}(0) \propto T^4$  expected for point nodes along the  $a$  axis [21]. Moreover, an accompanying  $T^3$  dependence of the electronic specific heat could not be confirmed from measurements above  $0.41 \text{ K}$  [Fig. 2(a) inset]. When fitting  $\lambda_{bc}(T)$  to a single-gap  $s$ -wave BCS model [34], with  $\Delta_{bc}$  as an adjustable parameter, we infer a much smaller gap than the BCS value of  $\Delta_{bc}(0) = 1.76k_B T_c$ . The small SC gap value may correspond to the minimum of a single anisotropic gap or the smallest gap of a multigap state. These results highlight the challenges when attempting to draw conclusions about the SC gap structure from fits of the temperature dependence of the magnetic penetration depth or thermodynamic quantities.

By contrast, a clear indication of the gap structure in  $\text{LaNiC}_2$  is provided by the low- $T$  magnetic field dependence of  $\lambda_{bc}$ , which is displayed in Fig. 2(b). The linear growth of  $\lambda_{bc}$

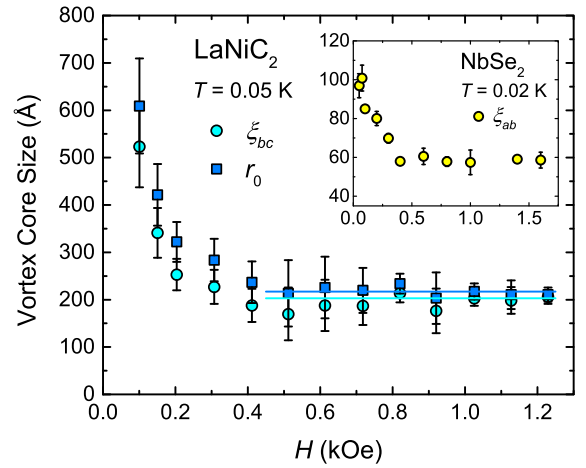


FIG. 3. Magnetic field dependence of  $r_0$  and  $\xi_{bc}$  in  $\text{LaNiC}_2$  for  $T = 0.05 \text{ K}$ . Inset: Magnetic field dependence of  $\xi_{ab}$  in  $\text{NbSe}_2$  for  $T = 0.02 \text{ K}$  [35].

with increasing  $H$  and the change in slope above  $H \sim 0.4 \text{ kOe}$  resemble the behavior of  $\lambda_{ab}(H)$  in the two-gap  $s$ -wave superconductor  $\text{NbSe}_2$  [35]. We note that  $\lambda$  exhibits no field dependence in a single fully gapped  $s$ -wave superconductor below  $H/H_{c2} \sim 0.5$  [36,37] and displays a sublinear dependence on field in a superconductor with gap nodes [38]. In  $\text{NbSe}_2$ , the initial steep linear- $H$  increase of  $\lambda_{ab}$  is attributed to the delocalization of loosely bound quasiparticle (QP) vortex core states associated with a small full energy gap on one of the conduction-electron bands. The delocalization results from an increased overlap of the bound QP states of neighboring vortices, which occurs due to the increase in vortex density at higher field. This modifies  $B(\mathbf{r})$  around the vortex cores and the fitted value of  $\lambda_{ab}$  (or  $\lambda_{bc}$ ). The “true” magnetic penetration depth for  $\text{LaNiC}_2$  is the extrapolated value  $\lambda_{bc}(T \rightarrow 0, H \rightarrow 0)$ , determined to be  $1548 \pm 24 \text{ \AA}$  from the linear fit of the low-field data presented in Fig. 2(b).

The delocalization of QP core states in  $\text{NbSe}_2$  at low  $T$  leads to a rapid decrease in  $r_0$  (and  $\xi_{ab}$ ) with increasing  $H$ , before saturating at higher fields where the vortex structure is controlled by the larger full SC gap on a different conduction band [35]. This is accompanied by a reduction in the slope of the linear- $H$  dependence of  $\lambda_{ab}$ . The saturation of the core size is due to the QP core states being more tightly bound to the smaller vortices associated with the larger gap. As shown in Fig. 3, the field dependence of the vortex core size in  $\text{LaNiC}_2$  at low  $T$  exhibits a behavior similar to that of  $\text{NbSe}_2$ , which is distinct from the behavior of the core size in a single-gap  $s$ -wave superconductor [36]. As expected, the low-field value of  $\xi_{bc}$  above the lower critical field ( $H_{c1} \sim 0.1 \text{ kOe}$ ) is close to the calculated value  $\xi_{bc} = [\Phi_0 / 2\pi H_{c2}^{\parallel a}]^{1/2} \approx 464 \text{ \AA}$ . We note that the weak field dependence of the core size at moderate fields is consistent with recent calculations for a two-band superconductor with large interband pairing [39].

To explore the existence of the two distinct SC gaps in more detail, we have fit the temperature dependence of the normalized low-field superfluid density,  $\lambda_{bc}^2(0)/\lambda_{bc}^2(T)$ , to a two-band, weak-coupling BCS model described in Appendix F. Techniques that measure the temperature

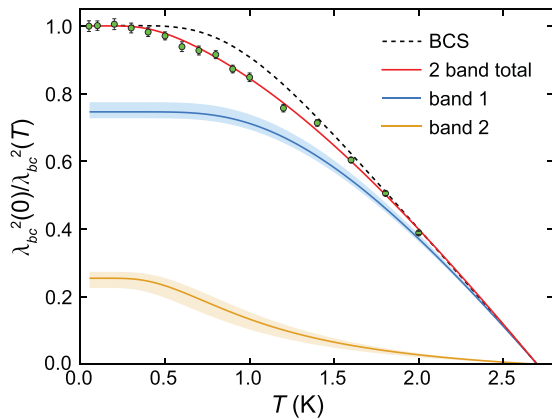


FIG. 4. Temperature dependence of the normalized superfluid density,  $\lambda_{bc}^2(0)/\lambda_{bc}^2(T)$ , in  $\text{LaNiC}_2$  for  $H = 150$  Oe. Circles denote  $\mu\text{SR}$  data points and error bars give the standard error at each temperature. The dashed curve is the superfluid density from single-band BCS theory. The upper solid curve is the total superfluid density in the two-band model, with contributions from the individual bands shown below it. Shaded areas denote the  $1\sigma$  uncertainty regions associated with the model fit. Fit parameters are given in Table I of Appendix F.

dependence of *absolute* superfluid density, such as  $\mu\text{SR}$ , directly probe the thermal excitation of quasiparticles across the energy gaps, with the two-band fit revealing the underlying energy gaps in a tightly constrained manner. As shown in Fig. 4, the single-band BCS curve does not adequately capture the measured superfluid density. The two-band model, however, provides a very good fit, and allows the contributions from the individual bands to be resolved. The range of temperature over which the thermally activated behavior of each band appears to be temperature independent is indicative of the energy gap in each band. From the detailed temperature dependence of the energy gaps (see Fig. 14, Appendix F) we infer zero-temperature gap ratios  $\Delta_i(0)/k_B T_c$  of 1.82 and 0.77, respectively, and a pairing strength in the subdominant band that is over an order of magnitude weaker than in the dominant band. We note that fits of the data in Fig. 15 to a two-superconductor model confirm the absence of a second superconducting phase in our  $\text{LaNiC}_2$  sample (see Appendix F).

Figure 5 shows ZF- $\mu\text{SR}$  asymmetry spectra for our  $\text{LaNiC}_2$  single crystals. These spectra are reasonably described by the same function applied in the earlier ZF- $\mu\text{SR}$  study of a polycrystalline sample [3]:

$$A(t) = A_0 G_{\text{KT}}(\sigma, t) \exp(-\Lambda t) + A_{\text{bg}}, \quad (2)$$

which consists of a relaxing term caused by the sample and a constant  $A_{\text{bg}}$  due to muons stopping in the Ag backing plate/sample holder. Here  $G_{\text{KT}}(\sigma, t)$  is a static Gaussian Kubo-Toyabe function [40]. The ZF- $\mu\text{SR}$  spectra were analyzed assuming only the relaxation rate  $\Lambda$  changes with temperature and with nearly equivalent values of  $A_0$  and  $A_{\text{bg}}$  determined from weak TF- $\mu\text{SR}$  measurements in the Meissner state. The fits yield  $\sigma = 0.104 \pm 0.002 \mu\text{s}^{-1}$  and the variation of  $\Lambda$  with temperature displayed in the inset of Fig. 5. Also shown is the increase of the ZF- $\mu\text{SR}$  relaxation rate reported in Ref. [3], which corresponds to a characteristic

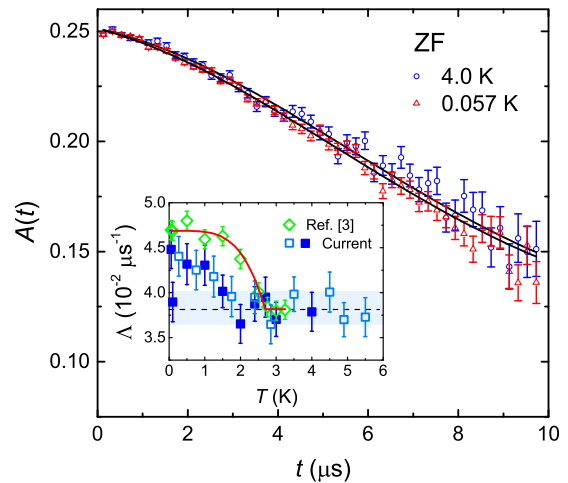


FIG. 5. Representative ZF- $\mu\text{SR}$  asymmetry spectra. The solid curves are fits to Eq. (2). Inset: Temperature dependence of the exponential ZF relaxation rate  $\Lambda$ . The open and solid squares correspond to two independent measurements of the  $\text{LaNiC}_2$  single crystals. The open diamonds are the exponential relaxation rate measured previously in polycrystalline  $\text{LaNiC}_2$  [3]. The dashed horizontal line denotes the average value of  $\Lambda$  above  $T_c$ ,  $\langle \Lambda \rangle_N$ , for each data set. The data set from Ref. [3] and that denoted by the solid squares have been shifted vertically upward so that  $\langle \Lambda \rangle_N$  for all three data sets coincide.

field strength of 0.10 G. While the error bars and scatter of our data are greater, an increase of  $\Lambda$  is observed at lower temperature.

The occurrence of spontaneous fields in  $\text{LaNiC}_2$  is apparently sample dependent. In addition to the previous results for a polycrystalline sample [3], an extremely small  $c$ -axis aligned spontaneous magnetization ( $\approx 10^{-5}$  G) far below the sensitivity of ZF- $\mu\text{SR}$  has been observed to appear in a single crystal at  $T_c$ , but not in a second single crystal investigated in the same study [41]. The situation of  $\text{LaNiC}_2$  somewhat resembles the lower TRS breaking SC phase of  $\text{UPt}_3$ , where weak spontaneous internal fields appearing at  $T_c$  were first detected by ZF- $\mu\text{SR}$  [25], but not later in higher quality single crystals [42,43]. In TRS breaking superconductors, intrinsic spontaneous magnetism is generated near the surface and by impurities and defects that disturb the SC order parameter [44]. Our measurements and those of Ref. [3] are not sensitive to spontaneous currents at the surface, as the mean stopping depth of the muons in  $\text{LaNiC}_2$  ( $\approx 0.2$  mm) far exceeds the magnetic penetration depth. We attribute the onset of weak internal fields at a lower temperature in our single crystals to the width of the SC transition. While magnetization measurements show a diamagnetic response beginning at 2.7 K, the zero-field cooled curve does not saturate until  $\approx 1.8$  K [see Fig. 10(a), Appendix C]. Given the small increase of the ZF- $\mu\text{SR}$  relaxation rate that is observed, it is likely that our experiments are not sensitive to the intrinsic spontaneous magnetism until sufficient spontaneous currents are formed around the sample inhomogeneities. We note that spontaneous internal fields are observed at a temperature substantially lower than  $T_c$  in ZF- $\mu\text{SR}$  studies of other TRS breaking superconductors with broad SC transitions [9,45].

#### IV. CONCLUSION

In summary, we have demonstrated the existence of two full SC gaps in  $\text{LaNiC}_2$  via detection of the field dependence of the magnetic field distribution at low temperatures in the vortex state of single crystals. Combined with supporting evidence for TRS breaking in the same sample, the nodeless two-gap SC state in  $\text{LaNiC}_2$  is compatible with interorbital equal-spin Cooper pairing [22–24].

#### ACKNOWLEDGMENTS

We thank Manfred Sigrist for insightful discussions and the staff of TRIUMF's Centre for Molecular and Materials Science for technical support. J.E.S., S.R.D., D.M.B. and E.M. acknowledge support from the Natural Sciences and Engineering Research Council of Canada. This research is also supported by the Japan Society for the Promotion of Science KAKENHI under Grants No. JP15K05156 and No. JP15KK0149.

#### APPENDIX A: POWDER X-RAY-DIFFRACTION SPECTRUM OF $\text{LaNiC}_2$

X-ray-diffraction (XRD) measurements were performed on one of the single crystals of  $\text{LaNiC}_2$  ground to a fine powder using a conventional x-ray diffractometer (RINT-2200, Rigaku Co., Ltd) equipped with a Cu target source. In addition to sharp Bragg peaks associated with  $\text{LaNiC}_2$ , the XRD spectrum (Fig. 6) shows three low intensity peaks associated with a  $\text{La}_2\text{Ni}_5\text{C}_3$  secondary phase occupying  $\approx 5\%$  of the sample. The lattice parameters for  $\text{LaNiC}_2$  determined from the XRD spectrum are  $a=3.9578$  Å,  $b=4.5616$  Å, and  $c=6.2001$  Å, which are in good agreement with literature values [15,19].

#### APPENDIX B: POWDER X-RAY-DIFFRACTION SPECTRUM AND RESISTIVITY OF $\text{La}_2\text{Ni}_5\text{C}_3$

Previous studies show that  $\text{La}_2\text{Ni}_5\text{C}_3$  is nonmagnetic and does not exhibit superconductivity down to 1.8 K [46,47]. To

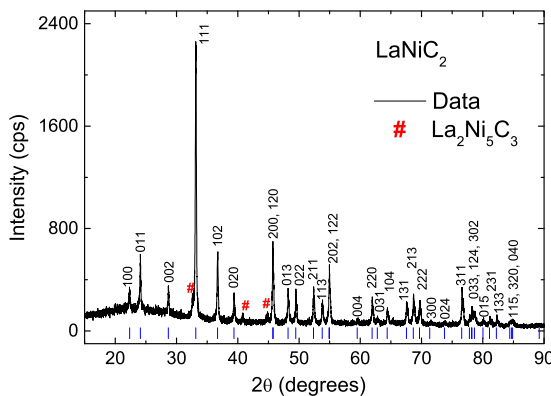


FIG. 6. Powder x-ray-diffraction (XRD) spectrum of  $\text{LaNiC}_2$ . The blue vertical lines indicate the calculated Bragg peak positions for  $\text{LaNiC}_2$ , which crystallizes in the orthorhombic  $Amm2$  space group. The three low intensity XRD Bragg peaks labeled with the pound sign are associated with an  $\approx 5\%$  secondary phase of  $\text{La}_2\text{Ni}_5\text{C}_3$ , which crystallizes in the tetragonal  $P4/mbm$  space group.

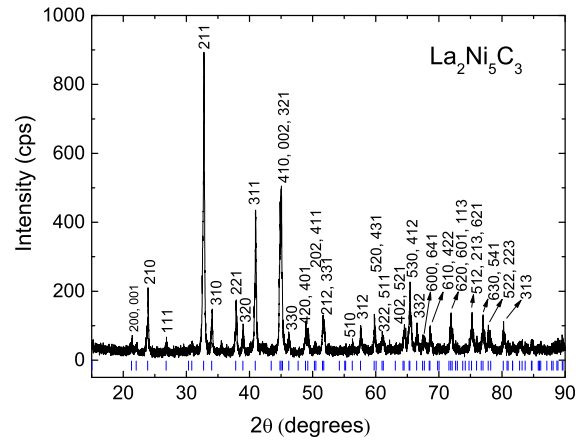


FIG. 7. Powder x-ray-diffraction (XRD) spectrum of  $\text{La}_2\text{Ni}_5\text{C}_3$ . The blue vertical lines indicate the calculated Bragg peak positions for  $\text{La}_2\text{Ni}_5\text{C}_3$ , which crystallizes in the tetragonal  $P4/mbm$  space group. The lattice parameters for  $\text{La}_2\text{Ni}_5\text{C}_3$  determined from the XRD spectrum are  $a=b=8.3266$  Å and  $c=4.0244$  Å.

determine whether superconductivity exists at lower temperatures, we synthesized a polycrystalline sample of  $\text{La}_2\text{Ni}_5\text{C}_3$ . A powder XRD spectrum of the  $\text{La}_2\text{Ni}_5\text{C}_3$  sample is shown in Fig. 7. As shown in Fig. 8, no superconducting transition is observed in the temperature dependence of the resistivity down to 0.11 K.

#### APPENDIX C: HEAT-CAPACITY AND MAGNETIZATION MEASUREMENTS OF $\text{LaNiC}_2$

Heat-capacity measurements were performed on a small piece of one of the  $\text{LaNiC}_2$  single crystals down to 0.4 K using a Quantum Design physical property measurement system. The temperature dependence of the heat capacity  $C(T)$  measured in zero and different applied magnetic fields is shown in Fig. 9(a). The bulk superconducting transition temperature  $T_c$  and the heat-capacity jump at  $T_c$  are determined in Fig. 9(b) by a procedure described in Ref. [48], which yields  $T_c \sim 2.7$  K and  $\Delta C/T_c \sim 9.66$  mJ mol $^{-1}$  K $^{-2}$ . These are consistent with literature values [15,16,19]. The dotted curve through the

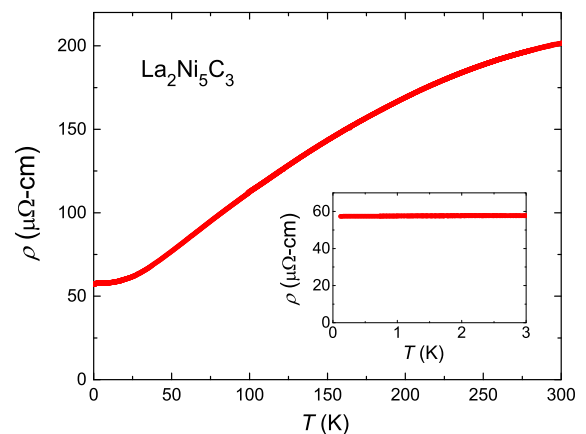


FIG. 8. Temperature dependence of the resistivity of polycrystalline  $\text{La}_2\text{Ni}_5\text{C}_3$  down to 0.11 K.

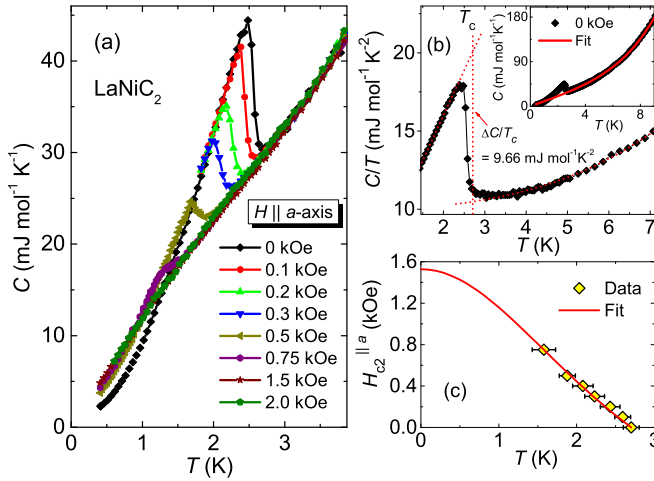


FIG. 9. (a) Temperature dependence of the heat capacity for different values of magnetic field applied parallel to the  $a$  axis. (b) The dotted lines duplicate a procedure described in Ref. [48] to estimate  $T_c$  and the heat-capacity jump  $\Delta C/T_c$  at  $T_c$ . Inset: Polynomial fit to the normal-state heat-capacity data for zero field over the temperature range 3.1–10.2 K, as described in the main text. (c) Temperature dependence of the upper critical field  $H_{c2}^{\parallel a}(T)$  estimated from the heat-capacity data in (a). The solid red curve is a fit to the data, which is described in the main text.

data above  $T_c$  in Fig. 9(b) comes from fitting the zero-field heat capacity from 3.1 to 10.2 K to a polynomial function,  $C(T) = \gamma T + \beta T^3 + \delta T^5$ , as shown in the inset of Fig. 9(b). The first term describes the electronic contribution to the heat capacity and the last two terms describe the lattice contribution. The fit yields  $\gamma \sim 9.9 \text{ mJ mol}^{-1} \text{ K}^{-2}$  and  $\beta \sim 0.066 \text{ mJ mol}^{-1} \text{ K}^{-4}$ . A fit of the data from 6 to 20 K instead yields  $\gamma \sim 7.7 \text{ mJ mol}^{-1} \text{ K}^{-2}$  and  $\beta \sim 0.142 \text{ mJ mol}^{-1} \text{ K}^{-4}$ , which are in good agreement with previously reported values [15,16,19]. The heat-capacity jump  $\Delta C/\gamma T_c \sim 0.98$  and 1.25 for  $\gamma \sim 9.9$  and  $7.7 \text{ mJ mol}^{-1} \text{ K}^{-2}$ , respectively.

Figure 9(c) shows the temperature dependence of the upper critical field  $H_{c2}^{\parallel a}$  estimated from the heat-capacity data in Fig. 9(a). The solid curve is a fit to the empirical

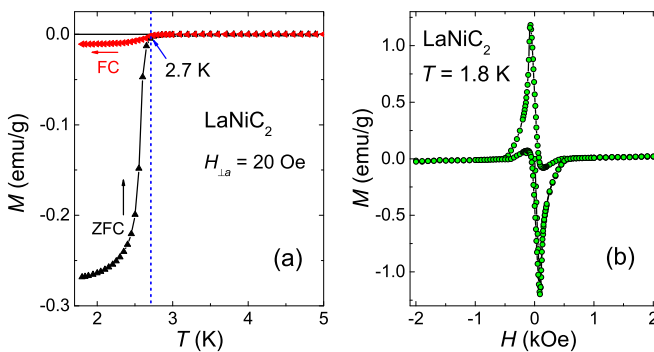


FIG. 10. (a) Temperature dependence of the dc magnetization down to 1.8 K measured for a magnetic field of 20 Oe applied perpendicular to the  $a$  axis under zero-field cooled (ZFC) and field cooled (FC) conditions. (b) Magnetic hysteresis ( $M$  vs  $H$ ) loop at 1.8 K.

relation  $H_{c2}^{\parallel a}(T) = H_{c2}^{\parallel a}(0)[1 - (T/T_c)^2]/[1 + (T/T_c)^2]$ , yielding values  $H_{c2}^{\parallel a}(0) = 1.53 \text{ kOe}$  and  $T_c = 2.7 \text{ K}$  that are in good agreement with a previous study of single crystal LaNiC<sub>2</sub> [28].

Measurements of the dc magnetization of LaNiC<sub>2</sub> were performed using a Quantum Design magnetic property measurement system. Zero-field cooled data show the onset of bulk superconductivity at  $\approx 2.7 \text{ K}$  [Fig. 10(a)]. Figure 10(b) shows a magnetization hysteresis loop for LaNiC<sub>2</sub> at 1.8 K. The magnetization versus magnetic field is characteristic of a type-II superconductor. The small hysteresis suggests any pinning of vortices by inhomogeneities in the sample is weak.

#### APPENDIX D: ANALYSIS OF THE TF- $\mu$ SR ASYMMETRY SPECTRUM

In the TF- $\mu$ SR configuration used for our experiments (see Fig. 11), the magnetic field  $\mathbf{H}$  was applied parallel to the muon beam momentum  $\mathbf{p}_\mu$  ( $z$  direction) along the  $a$  axis of the LaNiC<sub>2</sub> single crystals and the initial muon spin polarization  $\mathbf{P}(t=0)$  was rotated perpendicular to the applied field (in the  $x$  direction). The TF- $\mu$ SR asymmetry spectrum  $A(t) = a_0 P_x(t)$  is the sum of sample and background contributions

$$A(t) = A_s(t) + A_{bg}(t). \quad (\text{D1})$$

The first term originates from muons that stop in the LaNiC<sub>2</sub> single crystals. The second term originates from muons that stop outside the sample in the Ag backing plate or sample holder. Muons stopping in the sample and those stopping in the Ag backing plate/sample holder sense a distribution of nuclear dipole fields that cause depolarization of the TF- $\mu$ SR signal. Above  $T_c$ , the TF- $\mu$ SR asymmetry spectrum is well described by the sum of two Gaussian damped cosine functions:

$$A(t) = A_s \exp(\sigma_s^2 t^2) \cos(2\pi \nu_s t + \Phi) + A_{bg} \exp(\sigma_{bg}^2 t^2) \cos(2\pi \nu_{bg} t + \Phi). \quad (\text{D2})$$

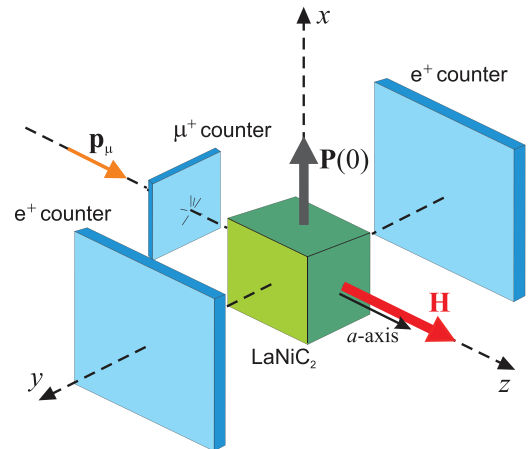


FIG. 11. Schematic of the geometry for the TF- $\mu$ SR experiments. The time evolution of the muon spin polarization  $P_x(t)$  is monitored via detection of the muon decay positrons in a pair of counters positioned on opposite sides of the sample.

The precession frequencies  $\nu_i$  ( $i = s, \text{bg}$ ) are a measure of the mean local field  $B_i$  sensed by the muon, where  $\nu_i = (\gamma_\mu/2\pi)B_i$  and  $\gamma_\mu/2\pi = 13.5539$  MHz/kG is the muon gyromagnetic ratio. The parameter  $\Phi$  is the initial phase of the muon spin polarization relative to the positron counter axis ( $y$  axis), which depends on the degree of Larmor precession of the muon spin in the applied field before reaching the sample.

Below  $T_c$ , the muons stopping in  $\text{LaNiC}_2$  also sense the spatial variation in magnetic field caused by a vortex lattice and the corresponding TF- $\mu$ SR asymmetry spectra were fit to the following two-component depolarization function:

$$A(t) = A_s \exp(\sigma_s^2 t^2) \int_0^\infty n(B) \cos(\gamma_\mu B t + \Phi) dB + A_{\text{bg}} \exp(\sigma_{\text{bg}}^2 t^2) \cos(2\pi \nu_{\text{bg}} t + \Phi), \quad (\text{D3})$$

where  $n(B') = \langle \delta[B' - B(\mathbf{r})] \rangle$  is the probability of a muon sensing a local magnetic field  $B$  in the  $z$  direction (parallel to the  $a$  axis of the  $\text{LaNiC}_2$  single crystals) at a position  $\mathbf{r}$  in the  $xy$  plane ( $bc$  plane). The spatial field profile associated with the vortex lattice  $B(\mathbf{r})$  was assumed to be described by Eq. (1). Below  $T_c$ , the depolarization function  $\exp(\sigma_s^2 t^2)$  accounts for the effects of both the nuclear dipole fields and vortex lattice disorder on the internal magnetic field distribution.

#### APPENDIX E: REPRESENTATIVE FOURIER TRANSFORMS OF TF- $\mu$ SR ASYMMETRY SPECTRA

Figures 12 and 13 show Fourier transforms of TF- $\mu$ SR asymmetry spectra.

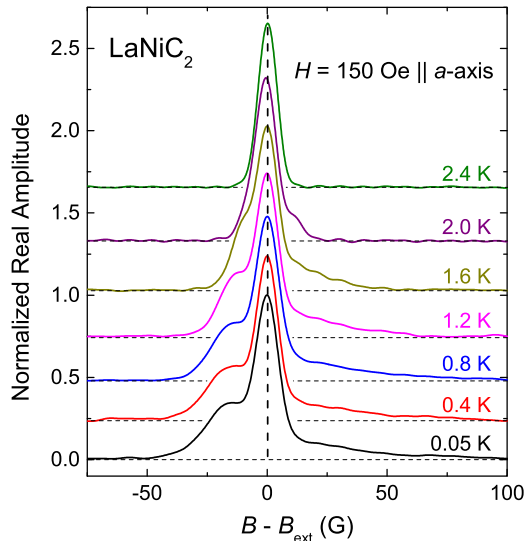


FIG. 12. Fourier transforms of the TF- $\mu$ SR asymmetry spectrum in  $\text{LaNiC}_2$  single crystals for a magnetic field of  $H = 150$  Oe applied parallel to the  $a$  axis. The horizontal axis is the difference between the local field sensed by the muon and the external field. The peak at  $B - B_{\text{ext}} = 0$  is a background signal originating from muons stopping outside the sample.

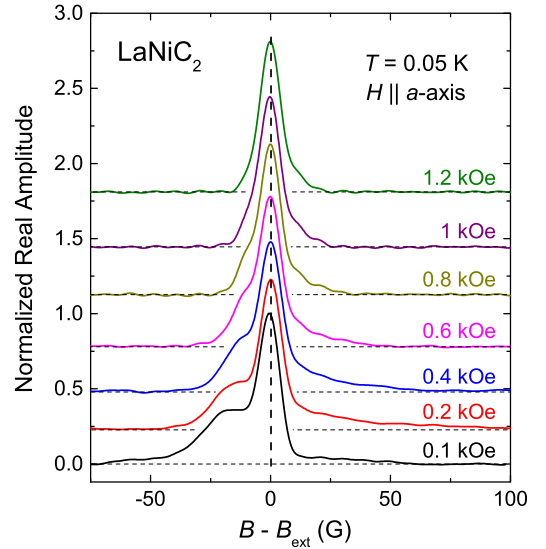


FIG. 13. Fourier transforms of the TF- $\mu$ SR asymmetry spectrum in  $\text{LaNiC}_2$  single crystals for  $T = 0.05$  K and different values of the magnetic field applied parallel to the  $a$  axis.

#### APPENDIX F: TWO-BAND BCS THEORY

##### 1. Gap equation

In the Matsubara formalism, the temperature-dependent gap equation for a weak-coupling superconductor is [49]

$$\Delta_{\mathbf{k}} = 2\pi T N_0 \sum_{\omega_n > 0} \left\langle V_{\mathbf{k}, \mathbf{k}'} \frac{\Delta_{\mathbf{k}'}}{\sqrt{\Delta_{\mathbf{k}'}^2 + \hbar^2 \omega_n^2}} \right\rangle_{\text{FS}} \quad (\text{F1})$$

where  $\omega_n = 2\pi T(n + \frac{1}{2})$  are the fermionic Matsubara frequencies,  $\Delta_{\mathbf{k}}$  is the gap parameter at wave vector  $\mathbf{k}$ ,  $N_0$  is the two-spin density of states,  $V_{\mathbf{k}, \mathbf{k}'}$  is the pairing interaction,  $\langle \dots \rangle_{\text{FS}}$  denotes an average over the Fermi surface, and  $\omega_0$  is a high-frequency cutoff.

The two-band superconductor describes situations in which the gap variation over the Fermi surface is approximately bimodal and can be approximated by two distinct gap scales,  $\Delta_1$  and  $\Delta_2$ , one for each band. As discussed in Ref. [49], the Fermi-surface average is replaced by a sum over bands, and the pairing interaction is parametrized by a  $2 \times 2$  symmetric matrix  $\lambda_{\mu\nu}$ , with the diagonal terms  $\lambda_{11}$  and  $\lambda_{22}$  describing intraband pairing, and the off-diagonal terms  $\lambda_{12} = \lambda_{21}$  describing the interband interaction. The gap equation then takes the simplified form

$$\Delta_\nu = \sum_{\mu=1,2} n_\mu \lambda_{\nu\mu} 2\pi T \sum_{\omega_n > 0} \frac{\Delta_\mu}{\sqrt{\Delta_\mu^2 + \hbar^2 \omega_n^2}}, \quad (\text{F2})$$

where the relative densities of states for each band,  $n_\mu$ , obey  $n_1 + n_2 = 1$ . For a given choice of parameters  $\{n_1, \lambda_{11}, \lambda_{22}, \lambda_{12}\}$ , Eq. (F2) is solved numerically, from which we obtain the temperature dependence of the gap parameters  $\Delta_1$  and  $\Delta_2$  (as shown, for example, in Fig. 14).

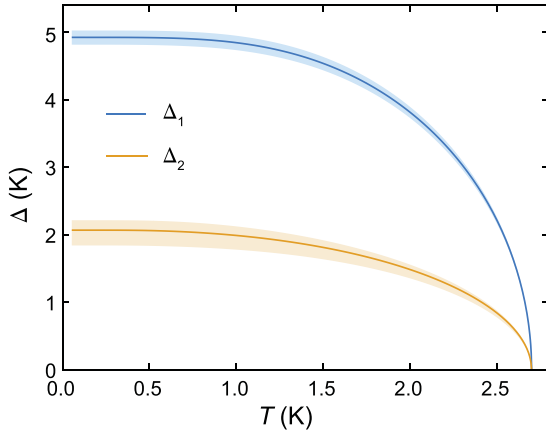


FIG. 14. Temperature dependence of the energy gaps,  $\Delta_1$  and  $\Delta_2$ , in the two-band model. Shaded areas denote the 1 sigma uncertainty regions associated with the model fit. The zero-temperature gap ratios,  $\Delta_i(0)/k_B T_{c_i}$ , are 1.82 and 0.77, respectively.

## 2. Superfluid density

Superfluid density is a thermal equilibrium property of the superconductor and is readily obtained within the Matsubara formalism once the energy gaps are known. For band  $\nu$ , the normalized superfluid density is

$$\rho_\nu(T) = \frac{\lambda_\nu^2(0)}{\lambda_\nu^2(T)} = \sum_{\omega_n > 0} \frac{\Delta_\nu^2}{(\Delta_\nu^2 + \hbar^2 \omega_n^2)^{3/2}}. \quad (\text{F3})$$

The total normalized superfluid density is a weighted sum of the contributions from each band:

$$\rho(T) = \gamma \rho_1(T) + (1 - \gamma) \rho_2(T), \quad (\text{F4})$$

where the weighting factor  $0 < \gamma < 1$  is determined by the plasma frequency imbalance between the bands. Note that  $\gamma$  is distinct from the density-of-states parameter  $n_1$ , as it includes Fermi velocity information:

$$\gamma = \frac{n_1 v_1^2}{n_1 v_1^2 + n_2 v_2^2}, \quad (\text{F5})$$

where  $v_1$  and  $v_2$  are the rms Fermi velocities of the two bands.

## 3. Fitting procedure and results

A least-squares optimization is used to search for best-fit parameters in the four-dimensional parameter space  $\{n_1, \lambda_{11}, \lambda_{22}, \lambda_{12}\}$ . For each parameter choice, the band-specific energy gaps and superfluid densities are determined at each of the experimental temperatures via numerical solution of Eqs. (F2) and (F3). As shown in Eq. (F4), the total superfluid density is a weighted combination of the band-specific superfluid densities. While the weighting coefficient  $\gamma$  is formally an additional fit parameter, a closed-form expression exists for its optimal value, so that it need not be included in the minimization search.  $\gamma_{\text{opt}}$  is found by minimizing the  $\chi^2$

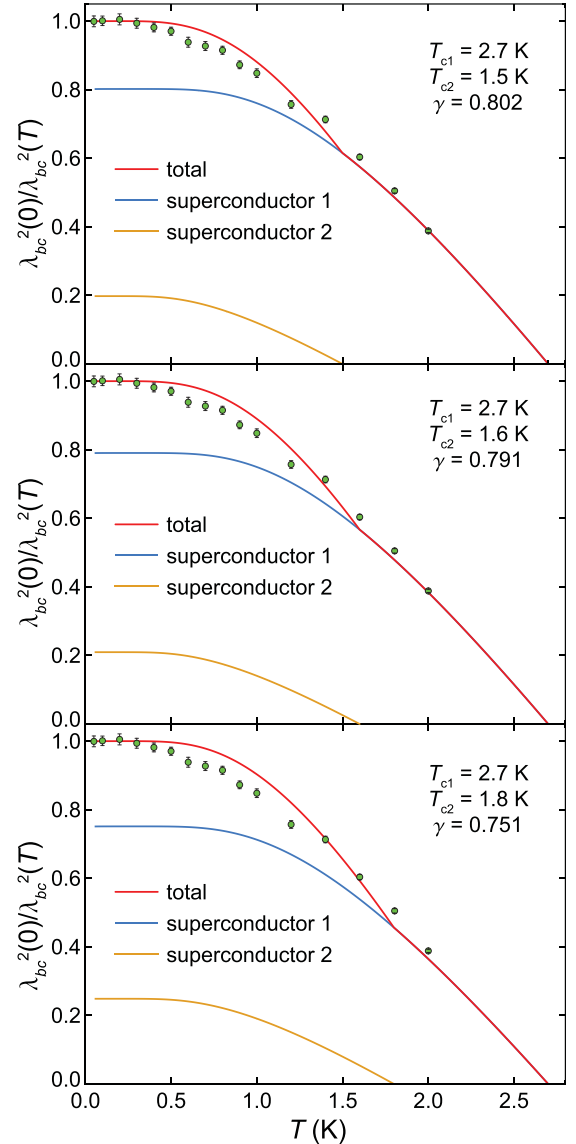


FIG. 15. Fits to the measured superfluid density for the two-phase superconductor model.  $T_{c1}$  is fixed at 2.7 K and  $T_{c2}$  is varied, taking on representative values of 1.5, 1.6, and 1.8 K in the three plots.

merit function

$$\begin{aligned} \chi^2 &= \left| \frac{\vec{\rho}_{\text{expt}} - \vec{\rho}_{\text{model}}}{\vec{\sigma}} \right|^2 \\ &= \left| \frac{\vec{\rho}_{\text{expt}} - \vec{\rho}_2 - \gamma \Delta \vec{\rho}}{\vec{\sigma}} \right|^2 \\ &= \frac{\gamma^2 |\Delta \vec{\rho}|^2 - 2\gamma \Delta \vec{\rho} \cdot (\vec{\rho}_{\text{expt}} - \vec{\rho}_2) + |\vec{\rho}_{\text{expt}} - \vec{\rho}_2|^2}{|\vec{\sigma}|^2} \end{aligned} \quad (\text{F6})$$

where  $\Delta \vec{\rho} = \vec{\rho}_1 - \vec{\rho}_2$ . Here the vector quantities encode the discrete temperature dependences of the various quantities, including experimental and model superfluid densities, and the measurement errors  $\vec{\sigma}$ . Minimizing with respect to  $\gamma$  we



TABLE I. Best-fit parameters and their uncertainties, for  $n_1 = 0.8$  and  $0.9$ .

Fit parameter	$n_1 = 0.9$	Uncertainty	$n_1 = 0.8$	Uncertainty
$\lambda_{11}$	0.77	$\pm 0.012$	0.71	$\pm 0.036$
$\lambda_{22}$	0.26	$\pm 0.013$	0.56	$\pm 0.023$
$\lambda_{12}$	0.23	$\pm 0.018$	0.22	$\pm 0.006$
$\gamma_{\text{opt}}$	0.747	$\pm 0.029$	0.746	$\pm 0.021$

obtain

$$\gamma_{\text{opt}} = \frac{\Delta \vec{\rho} \cdot (\vec{\rho}_{\text{expt}} - \vec{\rho}_2)}{|\Delta \vec{\rho}|^2}. \quad (\text{F7})$$

In practice, the optimization depends only weakly on the choice of density-of-states parameter  $n_1$ . Motivated by band-structure calculations [50,51] we estimate  $0.8 \lesssim n_1 \lesssim 0.9$  to be an appropriate physical choice, and present results in Table I for  $n_1 = 0.8$  and  $0.9$ . Figures 4 and 14 show the fits and gaps for  $n_1 = 0.8$ , which are practically indistinguishable from those for  $n_1 = 0.9$ . Note that while the  $\lambda_{22}$  parameter appears to vary sharply between the two cases, it is the combination  $n_2 \lambda_{22}$  that determines the intraband pairing strength in the second band, and this combination remains approximately constant. From this we conclude that the intrinsic pairing strength in the subdominant band is over an order of magnitude weaker than in the dominant band, and that interband pairing is important to the overall superconductivity.

#### 4. Two-phase superconductor

For comparison, we consider the superfluid density of a two-phase superconductor, which would apply if the material contained a secondary chemical phase that was also intrinsically superconducting. In this scenario, the two superconducting phases have different superconducting transition temperatures,  $T_{c1}$  and  $T_{c2}$ . Since there is no significant coupling between the phases, the temperature-dependent gap for each phase is the solution of a single-band BCS gap equation:

$$\Delta_v = 2\pi T N_0 V_0 \sum_{\omega_n > 0}^{\omega_0} \frac{\Delta_v}{\sqrt{\Delta_v^2 + \hbar^2 \omega_n^2}}. \quad (\text{F8})$$

The corresponding superfluid density is still given by Eq. (F3), and the effective superfluid density for the sample is still the weighted sum given by Eq. (F4). Fits to the measured absolute density are carried out by varying the  $\gamma$  parameter, which controls the relative weighting of the two phases.  $T_{c1}$  is fixed at 2.7 K and  $T_{c2}$  takes on representative values of 1.5, 1.6, and 1.8 K. Results are shown in Fig. 15. In each case, the best-fit superfluid densities in the two-phase scenario provide a much worse description of the data than the two-band model. Furthermore, the best fits require the secondary phase to contribute 20–25% of the total superfluid density. This is considerably greater than the 5% volume fraction of the known  $\text{La}_2\text{Ni}_5\text{C}_3$  phase, which in any case is nonsuperconducting.

- [1] E. Bauer and M. Sigrist, *Non-Centrosymmetric Superconductors: Introduction and Overview*, Lecture Notes in Physics Vol. 847 (Springer, New York, 2012).
- [2] M. Smidman, M. B. Salamon, H. Q. Yuan, and D. F. Agterberg, *Rep. Prog. Phys.* **80**, 036501 (2017).
- [3] A. D. Hillier, J. Quintanilla, and R. Cywinski, *Phys. Rev. Lett.* **102**, 117007 (2009).
- [4] P. K. Biswas, H. Luetkens, T. Neupert, T. Sturzer, C. Baines, G. Pascua, A. P. Schnyder, M. H. Fischer, J. Goryo, M. R. Lees, H. Maeter, F. Bruckner, H.-H. Klauss, M. Nicklas, P. J. Baker, A. D. Hillier, M. Sigrist, A. Amato, and D. Johrendt, *Phys. Rev. B* **87**, 180503(R) (2013).
- [5] R. P. Singh, A. D. Hillier, B. Mazidian, J. Quintanilla, J. F. Annett, D. McK. Paul, G. Balakrishnan, and M. R. Lees, *Phys. Rev. Lett.* **112**, 107002 (2014).
- [6] J. A. T. Barker, D. Singh, A. Thamizhavel, A. D. Hillier, M. R. Lees, G. Balakrishnan, D. McK. Paul, and R. P. Singh, *Phys. Rev. Lett.* **115**, 267001 (2015).
- [7] D. Singh, J. A. T. Barker, A. Thamizhavel, D. McK. Paul, A. D. Hillier, and R. P. Singh, *Phys. Rev. B* **96**, 180501(R) (2017).
- [8] T. Shang, M. Smidman, S. K. Ghosh, C. Baines, L. J. Chang, D. J. Gawryluk, J. A. T. Barker, R. P. Singh, D. McK. Paul, G. Balakrishnan, E. Pomjakushina, M. Shi, M. Medarde, A. D. Hillier, H. Q. Yuan, J. Quintanilla, J. Mesot, and T. Shiroka, *Phys. Rev. Lett.* **121**, 257002 (2018).
- [9] D. Singh, M. S. Scheurer, A. D. Hillier, and R. P. Singh, *Phys. Rev. B* **102**, 134511 (2020).
- [10] D. Singh, K. P. Sajilesh, J. A. T. Barker, D. McK. Paul, A. D. Hillier, and R. P. Singh, *Phys. Rev. B* **97**, 100505(R) (2018).
- [11] T. Shang, G. M. Pang, C. Baines, W. B. Jiang, W. Xie, A. Wang, M. Medarde, E. Pomjakushina, M. Shi, J. Mesot, H. Q. Yuan, and T. Shiroka, *Phys. Rev. B* **97**, 020502(R) (2018).
- [12] T. Shang, M. Smidman, A. Wang, L.-J. Chang, C. Baines, M. K. Lee, Z. Y. Nie, G. M. Pang, W. Xie, W. B. Jiang, M. Shi, M. Medarde, T. Shiroka, and H. Q. Yuan, *Phys. Rev. Lett.* **124**, 207001 (2020).
- [13] J. Quintanilla, A. D. Hillier, J. F. Annett, and R. Cywinski, *Phys. Rev. B* **82**, 174511 (2010).
- [14] S. P. Mukherjee and S. H. Curmoe, *Physica C* **499**, 6 (2014).
- [15] W. H. Lee, H. K. Zeng, Y. D. Yao, and Y. Y. Chen, *Physica C* **266**, 138 (1996).
- [16] V. K. Pecharsky, L. L. Miller, and K. A. Gschneidner, Jr., *Phys. Rev. B* **58**, 497 (1998).
- [17] Y. Iwamoto, Y. Iwasaki, K. Ueda, and T. Kohara, *Phys. Lett. A* **250**, 439 (1998).
- [18] S. Katano, K. Shibata, K. Nakashima, and Y. Matsubara, *Phys. Rev. B* **95**, 144502 (2017).
- [19] J. Chen, L. Jiao, J. L. Zhang, Y. Chen, L. Yang, M. Nicklas, F. Steglich, and H. Q. Yuan, *New J. Phys.* **15**, 053005 (2013).
- [20] I. Bonalde, R. L. Ribeiro, K. J. Syu, H. H. Sung, and W. H. Lee, *New J. Phys.* **13**, 123022 (2011).
- [21] J. F. Landaeta, D. Subero, P. Machado, F. Honda, and I. Bonalde, *Phys. Rev. B* **96**, 174515 (2017).
- [22] Z. F. Weng, J. L. Zhang, M. Smidman, T. Shang, J. Quintanilla, J. F. Annett, M. Nicklas, G. M. Pang, L. Jiao, W. B. Jiang, Y. Chen, F. Steglich, and H. Q. Yuan, *Phys. Rev. Lett.* **117**, 027001 (2016).

- [23] S. K. Ghosh, G. Csire, P. Whittlesea, J. F. Annett, M. Gradhand, B. Újfalussy, and J. Quintanilla, *Phys. Rev. B* **101**, 100506(R) (2020).
- [24] G. Csire, B. Újfalussy, and J. F. Annett, *Eur. Phys. J. B* **91**, 217 (2018).
- [25] G. M. Luke, A. Keren, L. P. Le, W. D. Wu, Y. J. Uemura, D. A. Bonn, L. Taillefer, and J. D. Garrett, *Phys. Rev. Lett.* **71**, 1466 (1993).
- [26] G. M. Luke, Y. Fudamoto, K. M. Kojima, M. I. Larkin, J. Merrin, B. Nachumi, Y. J. Uemura, Y. Maeno, Z. Q. Mao, Y. Mori, H. Nakamura, and M. Sgrist, *Nature (London)* **394**, 558 (1998).
- [27] Y. Aoki, A. Tsuchiya, T. Kanayama, S. R. Saha, H. Sugawara, H. Sato, W. Higemoto, A. Koda, K. Ohishi, K. Nishiyama, and R. Kadono, *Phys. Rev. Lett.* **91**, 067003 (2003).
- [28] Y. Hirose, T. Kishino, J. Sakaguchi, Y. Miura, F. Honda, T. Takeuchi, E. Yamamoto, Y. Haga, H. Harima, R. Settai, and Y. Ōnuki, *J. Phys. Soc. Jpn.* **81**, 113703 (2012).
- [29] J. E. Sonier, J. H. Brewer, and R. F. Kiefl, *Rev. Mod. Phys.* **72**, 769 (2000).
- [30] G. Morris and R. Heffner, *Physica B* **326**, 252 (2003).
- [31] A. Yaouanc, P. D. de Réotier, and E. H. Brandt, *Phys. Rev. B* **55**, 11107 (1997).
- [32] J. E. Sonier, *J. Phys.: Condens. Matter* **16**, S4499 (2004).
- [33] J. E. Sonier, *Rep. Prog. Phys.* **70**, 1717 (2007).
- [34] J. Halbritter, *Z. Physik* **243**, 201 (1971).
- [35] F. D. Callaghan, M. Laulajainen, C. V. Kaiser, and J. E. Sonier, *Phys. Rev. Lett.* **95**, 197001 (2005).
- [36] J. E. Sonier, F. D. Callaghan, R. I. Miller, E. Boaknin, L. Taillefer, R. F. Kiefl, J. H. Brewer, K. F. Poon, and J. D. Brewer, *Phys. Rev. Lett.* **93**, 017002 (2004).
- [37] R. Kadono, *J. Phys.: Condens. Matter* **16**, S4421 (2004).
- [38] J. E. Sonier, J. H. Brewer, R. F. Kiefl, G. D. Morris, R. I. Miller, D. A. Bonn, J. Chakhalian, R. H. Heffner, W. N. Hardy, and R. Liang, *Phys. Rev. Lett.* **83**, 4156 (1999).
- [39] A. Vargunin and M. A. Silaev, *Phys. Rev. B* **100**, 014516 (2019).
- [40] R. Kubo and T. Toyabe, in *Magnetic Resonance and Relaxation*, edited by R. Blinc (North-Holland, Amsterdam, 1967), p. 810.
- [41] A. Sumiyama, D. Kawakatsu, J. Gouchi, A. Yamaguchi, G. Motoyama, Y. Hirose, R. Settai, and Y. Ōnuki, *J. Phys. Soc. Jpn.* **84**, 013702 (2015).
- [42] P. Dalmas de Réotier, A. Huxley, A. Yaouanc, J. Flouquet, P. Bonville, P. Imbert, P. Pari, P. C. M. Gubbens, and A. M. Mulders, *Phys. Lett. A* **205**, 239 (1995).
- [43] W. Higemoto, K. Satoh, N. Nishida, A. Koda, K. Nagamine, Y. Haga, E. Yamamoto, N. Kimura, and Y. Onuki, *Physica B* **281–282**, 984 (2000).
- [44] M. Sgrist, *AIP Conf. Proc.* **789**, 165 (2005).
- [45] A. Bhattacharyya, D. Adroja, N. Kase, A. Hillier, J. Akimitsu, and A. Strydom, *Sci. Rep.* **5**, 12926 (2015).
- [46] Y. Kato, M. Kosaka, and N. Mōri, *AIP Conf. Proc.* **850**, 1099 (2006).
- [47] W. Jeitschko, M. H. Gerst, R.-D. Hoffmann, and S. Lee, *J. Less-Common Met.* **156**, 397 (1989).
- [48] S. L. Bud'ko, N. Ni, and P. C. Canfield, *Phys. Rev. B* **79**, 220516(R) (2009).
- [49] V. G. Kogan, C. Martin, and R. Prozorov, *Phys. Rev. B* **80**, 014507 (2009).
- [50] A. Subedi and D. J. Singh, *Phys. Rev. B* **80**, 092506 (2009).
- [51] I. Hase and T. Yanagisawa, *J. Phys. Soc. Jpn.* **78**, 084724 (2009).